Experimental and Numerical Investigation of a Shock Wave Impingement on a Cylinder

A. Brosh,* M. I. Kussoy,† and C. M. Hung†
NASA Ames Research Center, Moffett Field, California

This paper presents an experimental study and a numerical simulation of the impingement of an oblique shock wave on a cylinder. The investigation was undertaken to attain two goals. The first goal was to experimentally investigate and document the complex three-dimensional shock wave and boundary-layer interaction occurring in practical problems, such as the shock-wave impingement from the Shuttle nose on an external fuel tank, and store interference on a supersonic tactical aircraft. The second goal was to carry out a comparison of experimental measurements and numerical computations of such complex flows. The experimental results revealed a complex flowfield with two separation zones, regions of cross flow, reflected shocks, and expansion fans. The numerical predictions agreed surprisingly well with the measured results, both on the surface and in the flowfield. However, some important flow details, such as the size and extent of the separation, and the reflected shock-wave system, were not predicted.

Introduction

THERE has always been great interest in the fluid dynamics community in techniques for predicting complex flows that have practical significance.[1] During the last several years, advances in computer speed and memory have made this goal attainable. At present, one limitation to its fulfillment is the accuracy of the turbulence models used to describe the flow. Obviously, the value of any turbulence model is measured by its ability to predict an existing flow numerically, so that the results are consistent with experimental measurements. The present paper describes such an investigation, in which a complex flow that has practical applications was documented both experimentally and computationally. One goal of this investigation was to obtain experimental results of sufficient accuracy and detail so that they would reveal important aspects of a certain class of flows that are encountered in practice and lead to an improved understanding of the details of such flows. A second and equally important goal was to compare these results with theoretical predictions to help assess the worth of the turbulence model used and, more importantly, to indicate specific areas where improvements in the computational procedures are critically needed.

The impingement of an oblique shock wave on a cylindrical body is typical of an entire class of practical aerodynamic flows. Some realistic examples are the impingement of the bow shock from the Shuttle nose on the wing leading edge, the wing shock impinging on an external fuel tank, store-wing interaction, store separation, missile launching from supersonic tactical airplanes, and sabot interaction with armor-piercing ammunition. In these examples, the shock impingement results in heat-transfer, stability, control, and force problems which could materially affect the performance of the body.

The main features of the above class of three-dimensional shock-wave/turbulence boundary-layer interaction flows are duplicated by the experiment shown in Fig. 1. The test body consists of a cusp-like nose, followed by a long cylindrical section aligned with a Mach 3, freestream flow. A wedge spanning the test section generates a planar shock wave that impinges on the cylinder. The shock-wave/turbulent boundary-layer interaction zone thus formed on the cylinder is the subject of this investigation. Experimental observations were made using oil-flow visualization and static-pressure measurements on the surface, and static and total pressure surveys on the plane of symmetry in the flowfield. Shadowgraphs were also taken of the interaction region.

Numerical computations of this flow are obtained in the present study using the time-dependent, thin-layer approximation of the three-dimensional, Reynolds-averaged Navier-Stokes equations which are solved using the mixed explicit-implicit scheme of MacCormack,[2] for flow over a cylinder at zero incidence. The turbulence model used is the two-layer, algebraic, eddy-viscosity model of Baldwin and Lomax.[3] The computations are compared with the experimental measurements, and conclusions are drawn concerning the ability of the code and turbulence model used to predict this type of flow.

Description of Experiment

The experiment was conducted in HRC1,[4] which is a blowdown tunnel with a 25.4×38.1 cm test section operating at Mach 3. The test configuration and coordinate system used are shown in Fig. 1. A modular cylindrical body, with a cusp-shaped nose to eliminate shock waves, was mounted on the centerline of the test section.

The cylinder was 1 m long and 5.08 cm in diameter, and was instrumented along one body ray ($\phi_{body} = 0$ deg) with 28 pressure taps. Additional pressure taps were placed at $\phi_{body} = 90$, 180, and 270 deg to verify flow symmetry. A short modular body section housed a traversing mechanism for a variety of probes, enabling them to be moved perpendicular to the model axis. A potentiometer was geared directly to the probe support for a direct readout of the probe position independent of any gear backlash. Precise axial placement of the various probes was achieved by moving the probe axially in the probe support and fixing it with a set screw.

A two-dimensional shock-wave generator, consisting of an $\alpha = 16$ deg wedge that spanned the tunnel width, was mounted at a vertical position $h = 6.5$ cm from the tunnel wall. The wedge thickness was 5.08 cm. The two-dimensionality of the shock was checked by shadowgraphs and geometrical calculations of the shock position.

Presented as Paper 83-1757 at the AIAA 16th Fluid and Plasma Dynamics Conference, Danvers, Mass., July 12-14, 1983; received Aug. 22, 1983; revision received July 31, 1984. This paper is declared a work of the U.S. Government and therefore is in the public domain.

*Senior NRC Research Associate; presently with Technion, Haifa, Israel. Member AIAA.

†Research Scientist. Member AIAA.

The cylindrical test body was fixed in position, leveled, and centered in the test section; its alignment was checked before each individual run. The cylinder support allowed the test body to be arbitrarily positioned axially (x) and circumferentially (ϕ). The change in the undisturbed boundary-layer height at the measured station, owing to the axial movement of the cylinder, was about 1.2% of the nominal boundary-layer height; this change was found to have a negligible effect on the measured results.

Surface pressures were obtained using strain-gage transducers. By rotating the cylinder $\Delta\phi = 10$ deg between runs (at a constant axial position), pressure data were obtained at a sufficiently large number of points on the surface to generate accurate contour plots.

The oil-flow visualization technique was used to obtain surface flow patterns. The surface was covered with a sheet of black Mylar with an adhesive backing and coated with the oil mixture. The tunnel was run until a surface flow pattern was established that did not vary with time. Subsequent to the run, the Mylar sheet was peeled off and placed on a flat backing board for photographing and evaluation.

Surveys of static and total pressure in the boundary layer were made in the windward ($\phi = 0$ deg) and leeward ($\phi = 180$ deg) planes of symmetry intersecting the cylindrical test body. Surveys were made at axial locations spaced at $\Delta x = 0.635$ cm in the interaction region and $\Delta x = 1.27$ cm upstream and downstream of this region. The probe-traversing mechanism could advance the probe in discrete Δy increments as small as 0.005 cm. These surveys were taken at a Reynolds number $Re_\ell = 18.2 \times 10^6$, based on the length of the cylindrical body.

Pitot pressures were measured on the windward and leeward symmetry planes by a rectangular probe 0.012 cm high by 0.1 cm wide. The static pressure probe was a cone-ogive-cone-cylinder with a diameter of 0.07 cm. Four static holes were drilled 90 deg apart and 0.305 cm from the probe tip, according to the criteria of Pinckney.[5] This probe has the advantage of being less sensitive to flow angularity than the conventional cone-cylinder probe.

Total temperature was assumed constant and equal to the freestream total temperature of 278 K. Previous measurements by Kussoy et al.[6] at the same test conditions indicated that the total temperature varied less than 0.5% through the boundary layer.

The experimental uncertainties in the mean flow data in the windward and leeward planes are $\pm 10\%$ for the static pressure (because of flow angularity), $\pm 6\%$ for static temperature, $\pm 12\%$ for density, $\pm 3\%$ for velocity, and $\pm 1\%$ for pitot pressure. The uncertainty in y is ± 0.01 cm.

Experimental Results and Discussion

Flowfield Description

The flowfield around the cylindrical body can be divided into four different regions (Fig. 1): 1) the windward region, where the shock impinges on the cylinder and is governed by the severe pressure gradients and shear stresses caused by the shock; 2) the leeward region, where the flow is generally separated, and is governed by the cross flow and the thickening of the boundary layer; 3) the upstream region, ahead of the shock, where the flow is undisturbed parallel to the body axis at Mach 3; and 4) the downstream region, behind the wedge expansion fan, where the flow is straightened by the expansion and the difference in boundary-layer thickness between the leeward and windward still causes some cross-flow effects.

Shadowgraphs obtained during the experiment show, on the leeward, the development of a thick boundary layer (≈ 3 cm) and the extensive upstream influence of the impinging shock. These shadowgraphs also show the planar shock wave and the expansion fan, verifying the existence of a region between them where the flow is at a constant angle to the body axis.

Oil-Flow Patterns and Their Interpretation

A basic understanding of the character of surface properties can be gained by observing the oil-flow patterns. Some of the discussion in this section draws conclusions based also on data measured in the flowfield (e.g., boundary-layer height, separation bubble size, and expansion fans); those conclusions will be discussed later. A typical oil-flow pattern from the unwrapped Mylar sheet is shown in Fig. 2 where the main features of the surface flow can be seen. On the windward ($\phi = 10$ deg), the oil patterns show two separation lines, S_1 and S_2, and a point of reattachment NR. The most upstream of the two lines, the one that originates at S_1, terminates on the leeward ($\phi = 180$ deg). The other, which originates at S_2, wraps around the body, changing its attitude from lateral to axial, and becomes the primary leeward separation line.‡ S_3 is the secondary leeward separation line. The pattern of two parallel separation lines on the leeward is typical of a cylinder at an angle of attack, and has been observed previously by Yanta and Wardlaw[9] and Boersen.[10] An additional feature is the intense cross flow on the sides of the body (10 deg $< \phi <$ 100 deg) between $x = 50$ and 60 cm, which is of the same magnitude as the axial flow in this region (evident from the lateral direction of the surface lines).

The leeward interaction flow (120 deg $< \phi <$ 180 deg) shows three distinct regions. The first region (between $x = 54$ and 60 cm) is characterized by a thick boundary layer and is almost stagnant. The flow direction in this region is very difficult to assess from the oil-flow results shown in Fig. 2. The adverse pressure gradient, which is fed laterally from the freestream to the vicinity of the wall, and the intense cross flow (with an angle of over 45 deg from the freestream) both contribute to the thickening of the boundary layer in this region. The middle region (between $x = 60$ and 70 cm) is characterized, as mentioned previously, by two separation lines similar to those on the back of a cylinder at an angle of attack (see Ref. 11).

The downstream region (from $x = 70$ cm and beyond) is affected by the expansion fan off the top of the wedge and is, therefore, of less interest. The straightening of the flow in this region weakens the separation lines which eventually disappear.

Surface Pressure

Surface static-pressure distributions were measured on axial rays spaced every $\Delta\phi = 10$ deg around the cylinder. The windward and leeward results are presented in Fig. 3. The main features of the windward profiles ($\phi = 0$ deg) are the pressure rise at the foot of the shock, the double hump in the high-pressure region, and the downstream pressure drop caused by the wedge-expansion fan. The second pressure maximum on the windward ray, at $x = 60$ cm, is not an aberration caused by scatter in the data. This second maximum was observed in all measurements independent of body movement using different pressure taps and different transducers. The leeward profile ($\phi = 180$ deg) shows a very small pressure rise, suggesting that this entire region is in a wake of separated flow. The extent of upstream influence can also be drawn from this profile, since the inviscid shock passes the back of the body at $x = 62$ cm, and the pressure rise begins at $x = 55$ cm, meaning about 6 upstream boundary-layer thicknesses of forward influence.

Surface-pressure contours display a graphic picture of where the pressure extrema and pressure gradients are of significant influence. Figure 4 shows the experimental surface-

‡There is some controversy about the definition of three-dimensional separation. One view holds that skin-friction lines that converge and form a line which passes through a saddle point form a separation line[7]; the other view holds that only if a sheet of fluid actually leaves the surface is the footprint of this sheet on the surface a separation line.[8] In this paper, for convenience, the first view is adopted, without casting any judgment on the correctness of either view.

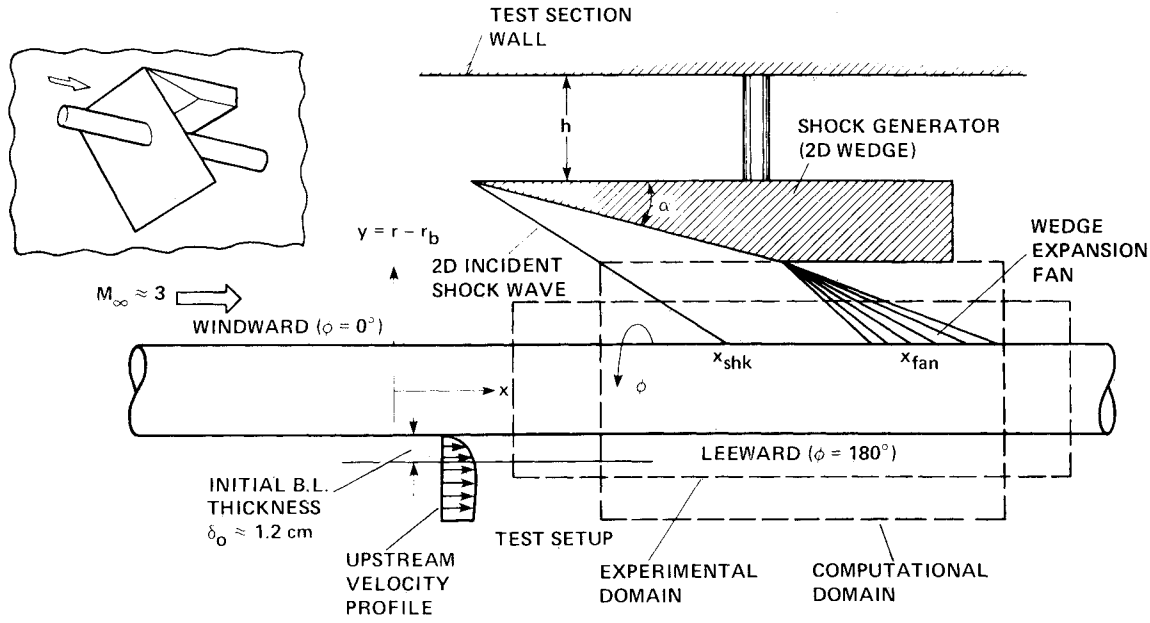

Fig. 1 Test setup with experimental and computational domains.

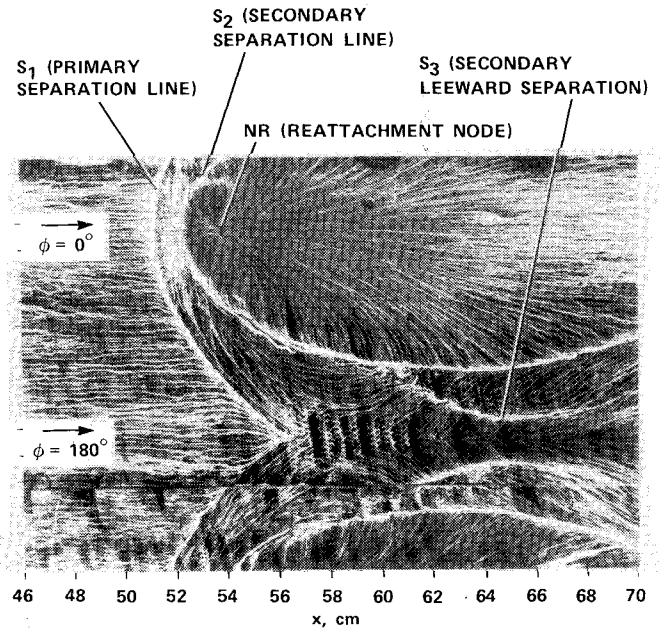

Fig. 2 Oil-flow pattern for 16-deg shock generator at $M=3$ and $P_{T\infty}=25$ psia.

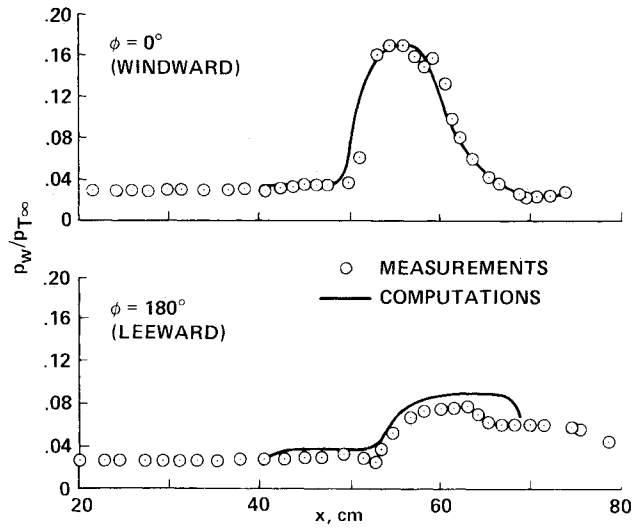

Fig. 3 Measured and predicted static-pressure distribution on a cylinder with impinging shock wave at $M=3$ and $P_{T\infty}=25$ psia.

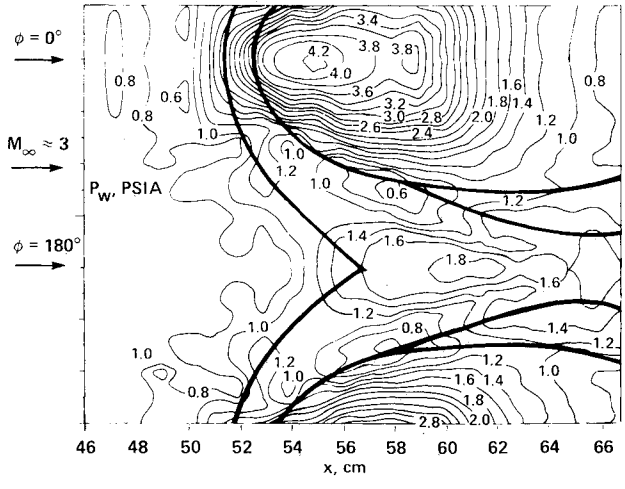

Fig. 4 Measured surface-pressure contours on a cylinder with impinging shock wave at $M=3$ and $P_{T\infty}=25$ psia.

pressure contours with the main features of the oil-flow pattern (bold lines). The severe pressure gradients at the foot of the shock ($x=52$ cm) on the windward ($\phi=0$ deg) are congruent with the dual separation lines in the oil-flow picture. Surprisingly, the contours show the same magnitude of pressure gradients in the lateral direction. These gradients are responsible for the severe cross flow which, in turn, causes a leeward separation, similar to that on a cylinder at an angle of attack, as was discussed previously. A somewhat unanticipated feature is the point of minimum pressure at $\phi=100$ deg and $x=58$ cm. This minimum occurs exactly where the leeward separation line bifurcates, and the resulting two lines of separation follow the two pressure valleys that lead downstream from this point. The surface-pressure gradients on the leeward are very small, also showing that the flow is of separated-wake type.

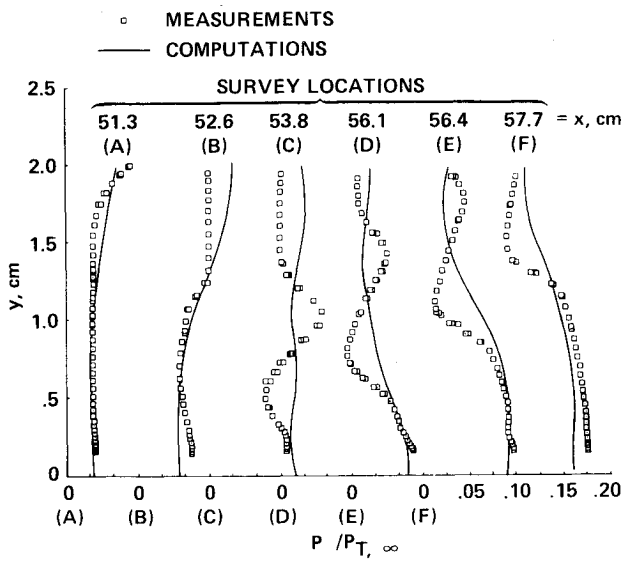

a) Static pressure.

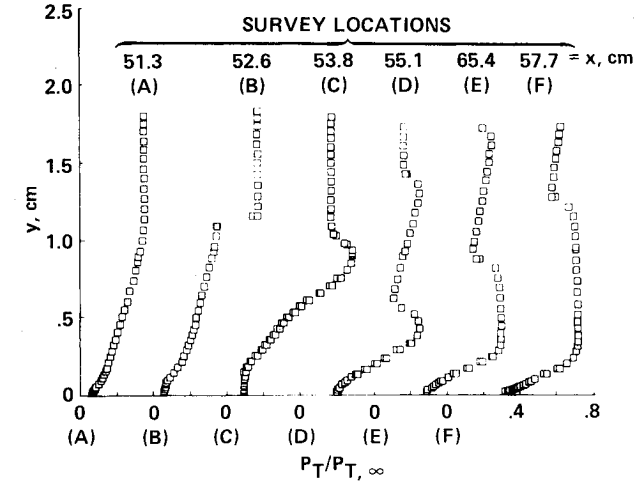

b) Total pressure.

Fig. 5 Measured and predicted pressure profiles on the windward plane of symmetry of a cylinder with impinging shock at $M=3$ and $P_{T\infty}=25$ psia.

Pressure Surveys

Additional details of this complex flowfield were obtained from pressure surveys taken on the windward and leeward planes of symmetry. Figure 5 shows the results of pressure surveys in six locations (A-F), representing the main flow features on the windward plane. Figure 5a shows the static pressure P, and Fig. 5b shows the total pressure P_T. Survey A ahead of the interaction shows the beginning of the static-pressure rise near the shock (Fig. 5a, $y=2$ cm), and the upstream boundary-layer edge, as picked up by the total-pressure profile (Fig. 5b, $y=1.2$ cm). Survey B hits the incident shock at the boundary-layer edge. Survey C traverses the bubble. The total pressure at C shows no change close to the surface, indicating the presence and extent of the bubble in this location; thereafter, the pressure decreases, indicating the presence of a local expansion fan (a "separation bubble expansion" since it originates from the bubble). Farther from the body, at $y=1.0$ cm, survey C encounters another shock, the "separation shock." Survey D, just behind the separation bubble, indicates the presence of yet another shock at $y=0.5$ cm, called the "recompression shock" for obvious reasons. Surveys E and F show the same shock-wave expansion-fan structure as it recedes from the body surface at a constant angle.

Pressure Contours

The symmetry plane flow structure is illustrated further in Fig. 6 which shows the static-pressure contours with the three shock waves superimposed. Points of interest in this figure are the two reflected shocks; the pressure hill behind the intersection of the incident shock and the separation shock; and the pressure valley between the two reflected shocks which indicates the existence of an expansion fan emerging from the separation bubble. The pressure peak at the wall behind the shock system is decaying fairly fast, because the wedge-expansion fan, from the wedge-ramp corner, hits the body at $x\approx 60$ cm.

Numerical Simulation

Thin-Layer Approximation

Figure 1 shows the computational domain, and the geometry used in the calculations. The basic equations of the present analysis are the time-dependent, compressible, mass-averaged Navier-Stokes equations. For our high-Reynolds-number flow, the viscous effects are confined to a thin layer

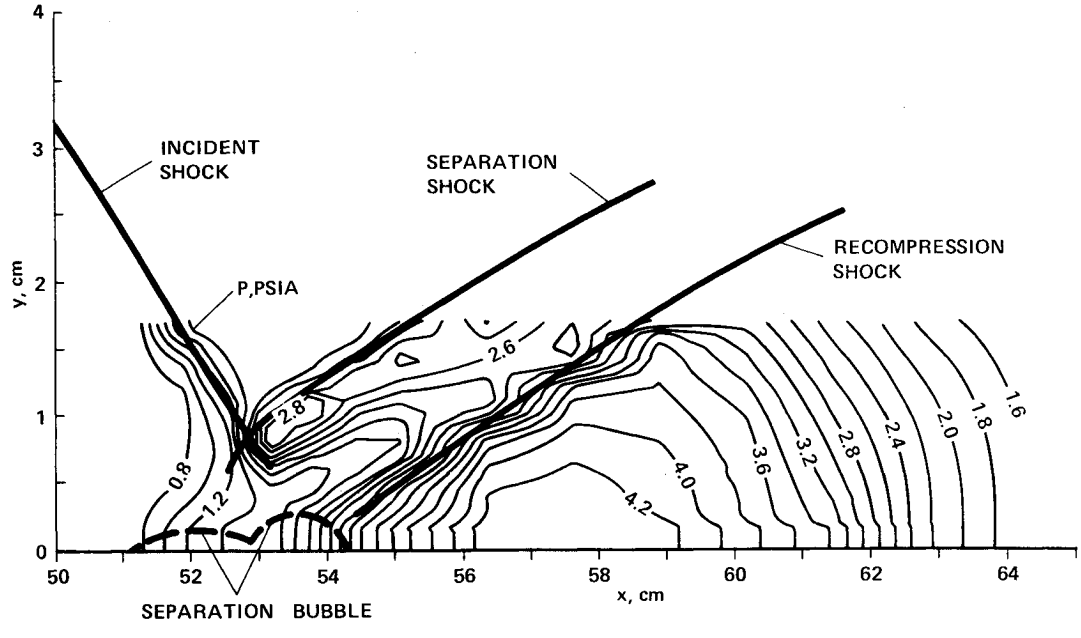

Fig. 6 Measured static-pressure contours on the windward plane at $M=3$ and $P_{T\infty}=25$ psia.

near the wall, and are associated with the derivative in the r direction. Consequently, all viscous terms associated with x and ϕ derivatives are neglected, while those with second derivatives in the r direction are retained. Written in transformed cylindrical coordinates, the thin-layer approximation of the Navier-Stokes equations is as follows:

$$\frac{\partial rU}{\partial t}+\frac{\partial rF}{\partial \xi}+\frac{\partial r(G-G_V)}{\partial \eta}+\frac{\partial rH}{r\partial \phi}+Q=0$$

where

$$\xi=x, \quad \eta=r-r_b(x)$$

and U represents the conservative variables. F, G, and H are the transport inviscid fluxes, G_V the thin-layer approximation of the transport viscous flux, and Q the forcing term as follows:

$$U=\begin{bmatrix}\rho\\ \rho u\\ \rho v\\ \rho w\\ \rho E\end{bmatrix}, \quad F=\begin{bmatrix}\rho u\\ \rho u^2+P\\ \rho uv\\ \rho uw\\ (\rho E+P)u\end{bmatrix}$$

$$H=\begin{bmatrix}\rho w\\ \rho uw\\ \rho vw\\ \rho w^2+P\\ (\rho E+P)w\end{bmatrix}, \quad G=\begin{bmatrix}\rho v'\\ \rho uv'-r_b'(x)P\\ \rho vv'+P\\ \rho wv'\\ (\rho E+P)v'\end{bmatrix}$$

$$G_V=\begin{bmatrix}0\\ \sigma_{rx}-r_b'(x)\sigma_{xx}\\ \sigma_{rr}-r_b'(x)\sigma_{rx}\\ \sigma_{r\phi}-r_b'(x)\sigma_{\phi x}\\ \theta_r-r_b'(x)\theta_x\end{bmatrix}, \quad Q=\begin{bmatrix}0\\ 0\\ -P-\rho w^2+\sigma_{\phi\phi}\\ \rho vw-\sigma_{r\phi}\\ 0\end{bmatrix}$$

$$v'=v-ur_b'(x)$$

In the above equations, u, v, w are the velocity components in the axial (x), radial (r), and azimuthal (θ) directions; ρ, P, and E are density pressure, and total specific energy, respectively; σ_{xx}, σ_{rr}, $\sigma_{\phi\phi}$, σ_{rx}, $\sigma_{r\phi}$, $\sigma_{\phi x}$, and θ_x, θ_r denote the thin-layer approximations of the viscous normal and shear stresses and heat flux components. The perfect-gas relation is used, and the molecular viscosity is evaluated by Sutherland's formula.

The flow is symmetrical in ϕ, and, hence, only a half-plane, 0 deg $\leq\phi\leq$ 180 deg, is considered. The mesh spacing in the x, r, and ϕ directions may vary independently. In the present study, the mesh was uniformly spaced at first in both the x and ϕ directions ($\Delta x=0.57$ cm and $\Delta\phi=5$ deg). In the r direction, a fine mesh spacing is used in the region near the body, $r_b\leq r\leq r_f$, to resolve the viscous forces (initial $\Delta y_f=1.24\times 10^{-2}$ cm), and coarse-mesh spacing is used in the outer region, $r_f\leq r\leq r_0$, where viscous effects are negligible (final $\Delta y_0=0.3$ cm). Both the fine and coarse meshes are geometrically stretched. A two-layer turbulence model developed by Baldwin and Lomax[3] is used. The numerical technique in this work is a mixed explicit-implicit scheme developed by MacCormack.[2] The program is coded for the treatment of general bodies of revolution, i.e., $r_b=f(x)$. However, in the present calculations $r_b'(x)$ is zero, and the geometry is reduced to the case of a circular cylinder. Details of the numerical procedure are described by Hung et al.[12-14]

Boundary Conditions

The calculations duplicated the geometry of the experiment, including the shock wave and the expansion generated by the wedge. The upstream conditions, including the Mach number M, boundary-layer thickness δ, and total pressure P_T, were input from the experimental data. A symmetry condition is applied at the $\phi=0$ and 180 deg planes. A zero-gradient boundary condition is used at the downstream boundary. The wall is assumed impermeable, and no-slip boundary conditions are used. The wall is adiabatic, and the wall pressure is evaluated using $\partial P/\partial r=0$ at $r=r_b$. In the present case, the first mesh point is close enough to the wall ($y=6.2\times 10^{-3}$ cm) so that this pressure condition is appropriate.

The impinging planar shock wave strikes the cylinder at an angle $\beta=34.5$ deg, and intercepts on the windward plane $\phi=0$ deg and $x=x_{\text{shk}}$. The expansion fan is generated at $x=x_{\text{fan}}$. Ahead of the plane shock the boundary conditions are equal to the freestream conditions (M_∞, ρ_∞, P_∞), and between the shock and expansion fan ($x>x_{\text{shk}}$) they are set at post-shock conditions (M_1, ρ_1, P_1). A simple Prandtl-Meyer expansion solution is used in the fan region ($x>x_{\text{fan}}$), and a uniform solution is used downstream of the expansion.

Comparison of Computations and Measurements

One of the main problems encountered repeatedly by the computation is the underprediction of the large experimentally observed separation bubble.[15,16] When the experimentally observed bubble is small, the disturbance it introduces into the

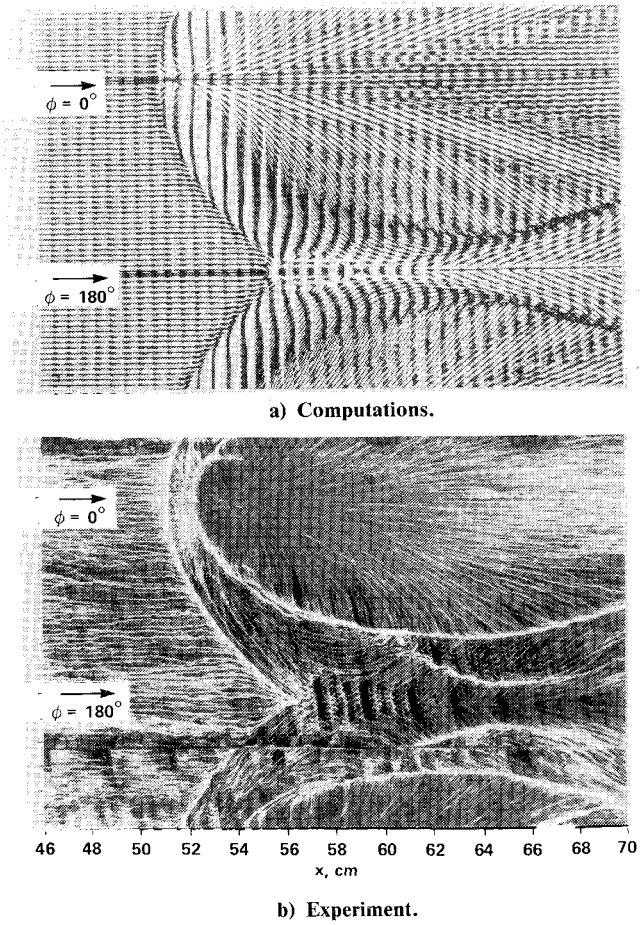

a) Computations.

b) Experiment.

Fig. 7 Comparison of computed surface-velocity pattern and experimental oil-flow picture.

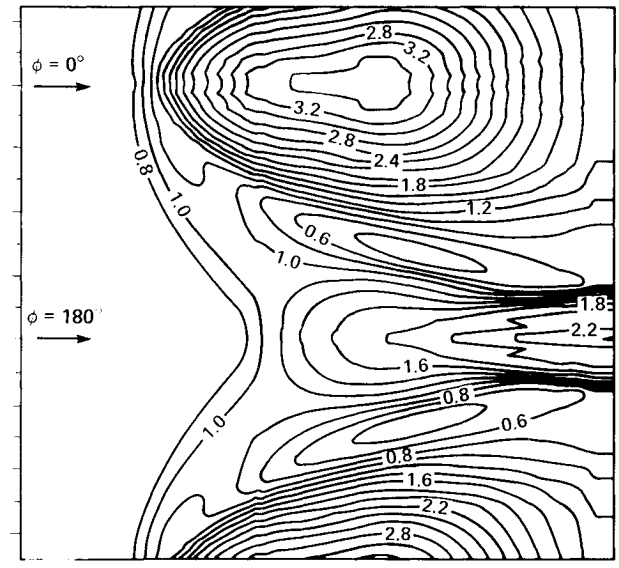

a) Computations.

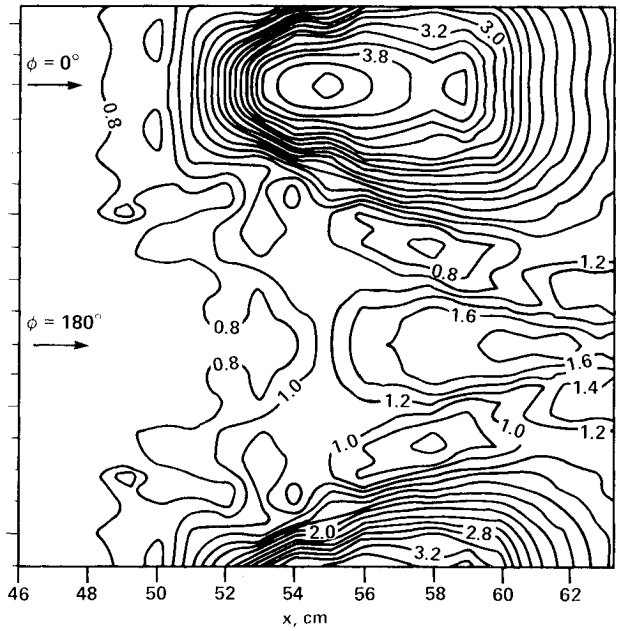

b) Measurements.

Fig. 8 Comparison of computed and measured pressure contours on the cylinder surface at $M=3$ and $P_{T\infty}=25$ psia.

flowfield is also small; hence, the shock pattern consists of one incident shock and one reflected shock. This simple case can be predicted by the calculations.[17] But when the observed separation bubble is large, introducing a large obstacle into the boundary layer, the resulting shock pattern and the separation features are more complex, and the calculations fail to predict the experimental observations. The comparison of computational and experimental surface properties is shown in Fig. 7. The computed surface limiting velocity vectors (i.e., velocity vectors at $y=6.2\times10^{-3}$ cm, the first grid point above the surface) are shown in Fig. 7a. These predict accurately the first upstream separation line and the overall flowfield features; however, discrepancies appear in two regions. The computed windward separation region ($\phi=0$ deg), represented by the reverse flow, is extremely small, resulting in one separation line only. Also, the separation line on the leeward, caused by the cross flow, occurs at too high a value of ϕ and consists of a single separation line only. In contrast, the experimental results presented in Fig. 7b show a much larger reversed-flow region on the windward ($\phi=0$ deg), resulting in two windward separation lines. Also, the leeward separation, caused by the cross flow, starts at a smaller ϕ and consists of two lines.

The calculated surface pressures fit the experiment very well on the windward ($\phi=0$ deg) and leeward ($\phi=180$ deg) lines, as can be seen from Fig. 3. The small deviation in the location of the pressure maximum on the windward is acceptable since the gradients are small. The maximum is almost constant, and is predicted within 5%. However, the second pressure maximum mentioned previously is not predicted by the calculations. The measured and computed surface-pressure contours (Fig. 8) have similar overall features. The location and intensity of the predicted pressure minimum at $\phi=100$ deg agree with the measurements. The main difference between the calculated and measured surface pressures is the calculated strong azimuthal pressure gradients near the leeward where the measurements show almost constant pressure.

The computed flowfield properties are shown in Fig. 9, which presents the pressure contours as calculated on the plane of symmetry. Comparing the windward calculations to the measured contours in Fig. 6, it is observed again that the general features of the flowfield are duplicated very well, especially when considering the complexity of the flowfield. However, because of the small computed separation bubble, the reflected shock structure is not predicted, and the pressure distribution is somewhat different. The pressure peak behind the intersection of the incident and separation shocks is missing in the calculations, no expansion fan is emerging from the bubble top, and the two reflected shocks merge into one. Figure 5a shows a comparison of the calculated and measured pressure profiles on the windward plane of symmetry. The dif-

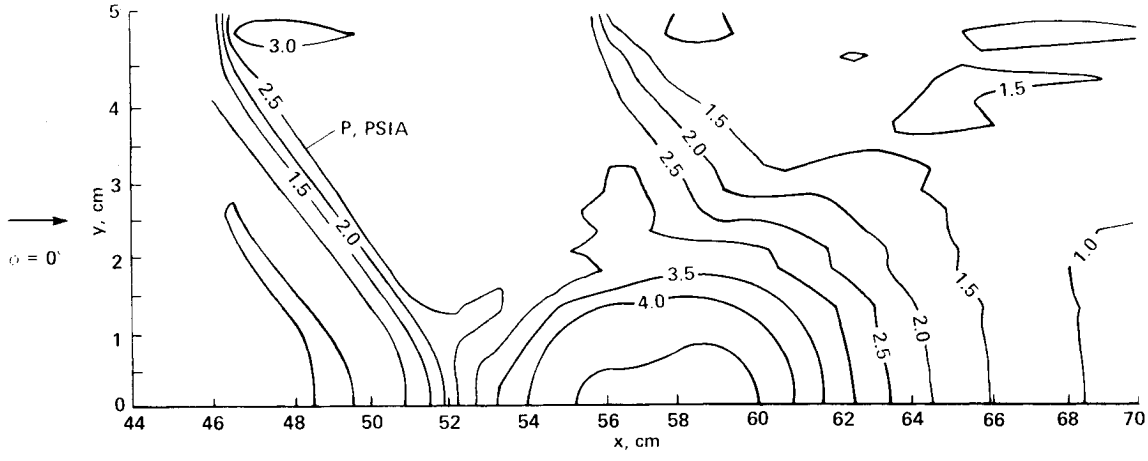

Fig. 9 Computed pressure contours on the plane of symmetry.

fusing effect of the computational grid on the shock is obvious from profiles A and B. The incident shock, which is very sharp in the measurements (and even sharper in the total pressure surveys; see, e.g., Fig. 5b, survey B), is captured by no less than five grid points and, therefore, is spread over almost one full boundary-layer thickness. The same effect is evident from profiles C, D, E, and F concerning the reflected shock. These profiles also substantiate the conclusion obtained from the surface-pressure contour plots, that the computations fail to resolve the expansion fan originating from the separation bubble.

Concluding Remarks

Experimental measurements of the complex three-dimensional flow were made. The flowfield includes shock waves, three-dimensional separation, and severe cross flow. A computer code, using the thin-layer approximation of the Navier-Stokes equations with a two-layer, eddy-viscosity turbulence model is used to predict this flow. The main experimental and computational results are listed below.

1) The incident shock wave is sufficiently strong to produce a large, double separation bubble. Two reflected shocks and an expansion fan are observed in the windward region. Wake-type flow with double separation is observed on the leeward. The surface-flow structure exhibited an intense lateral cross flow. This cross flow thickens the boundary layer and causes significant upstream influence on the leeward.

2) The computations predict the main features of the flow, including the surface-pressure distribution, the primary separation, and the upstream separation lines, as well as the cross flow and the extent of upstream influence. However, they underpredict the size of the separation bubble, and hence, miss some significant features of the flow on the windward, such as the secondary separation lines, the double shock reflection, and the bubble expansion fans. On the leeward, the computations exhibit too high a pressure recovery, the primary leeward separation is delayed, and the secondary separation is absent.

3) Two weaknesses in the computations are apparent. The first weakness is that the present eddy-viscosity turbulence model fails to predict the large experimentally observed bubble size. The second weakness is that the grid inherently smears the shock over several mesh points, thus reducing the gradients across it. Closer grid spacing improves the predicted surface-pressure results.

References

[1]Marvin, J. G., "Turbulence Modeling for Compressible Flows," NASA TM X-73187, 1977.

[2]MacCormack, R. W., "An Efficient Numerical Method for Solving the Time Dependent Compressible Navier-Stokes Equations at High Reynolds Number," NASA TM X-73129, 1976.

[3]Baldwin, B. S. and Lomax, H., "Thin Layer Approximation and Algebraic Model for Separated Turbulent Flow," AIAA Paper 78-257, Jan. 1978.

[4]Brosh, A. and Kussoy, M. I., "An Experimental Investigation of the Impingement of a Planar Shock Wave on an Axisymmetric Body at Mach 3," NASA TM 84410, 1983.

[5]Pinckney, S. F., "An Improved Static Probe Design," *AIAA Journal*, Vol. 12, April 1974, pp. 562-564.

[6]Kussoy, M. I., Horstman, C. C., and Acharya, M., "An Experimental Documentation of Pressure Gradient and Reynolds Number Effect on Compressible Turbulent Boundary Layers," NASA TM-78488, 1978.

[7]Peake, D. J. and Tobak, M., "Three Dimensional Interactions and Vortical Flows with Emphasis on High Speed," NASA TM-81169, 1980.

[8]Legendre, R., "Evolution Réguiliére ou Catastrophique d'Ecoulements Permanents Dependant de Paramétres," *La Recherche Aérospatiale*, No. 1982-4 Juillet-Août, 1982, pp. 225-232 (translated by M. Tobak, Jan. 1983).

[9]Yanta, W. J. and Wardlaw, A. B. Jr., "The Secondary Separation Region on a Body at High Angles of Attack," AIAA Paper 82-0343, Jan. 1982.

[10]Boersen, S., "Reynolds Number Effects on Pressure and Normal Force Distribution Along a Conically Pointed Circular Cylinder at Mach 2.3," NLR TR 75124-U, Sept. 1975.

[11]Peake, D. J. and Tobak, M., "Three Dimensional Flows About Simple Components at Angle of Attack," NASA TM-84226, 1982.

[12]Hung, C. M., "Numerical Solution of Supersonic Laminar Flow Over an Inclined Body of Revolution," *AIAA Journal*, Vol. 18, Aug. 1980, pp. 921-928.

[13]Hung, C. M. and Chaussee, D. S., "Numerical Solution of Supersonic Turbulent Flow Over an Inclined Ogive Cylinder Flare," *AIAA Journal*, Vol. 19, Sept. 1981, pp. 1139-1144.

[14]Hung,, C. M., "Impingement of an Oblique Shock Wave on a Cylinder," AIAA Paper 82-0025, Jan. 1982.

[15]Horstman, C. C., Kussoy, M. I., Coakley, T. J., Rubesin, M. R., and Marvin, J. G., "Shock Wave Induced Turbulent Boundary Layer Separation at Hypersonic Speeds," AIAA Paper 75-004, Jan. 1975.

[16]Kussoy, M. I., Viegas, J. R., and Horstman, C. C., "Investigation of a Three Dimensional Shock Wave Separated Turbulent Boundary Layer," *AIAA Journal*, Vol. 18, Dec. 1980, pp. 1447-1484.

[17]Mateer, G. G., Brosh, A., and Viegas, J. R., "A Normal Shock Wave Turbulent Boundary Layer Interaction at Transonic Speeds," AIAA Paper 76-161, Jan. 1976.